Clim Dyn (2014) 42:2783–2799
DOI 10.1007/s00382-014-2116-6

Climate mean, variability and dominant patterns of the Northern Hemisphere wintertime mean atmospheric circulation in the NCEP CFSv2

Peitao Peng · Arun Kumar · Bhaskar Jha

Received: 2 July 2013 / Accepted: 7 March 2014 / Published online: 26 March 2014

Abstract In this study, the climate mean, variability, and dominant patterns of the Northern Hemisphere wintertime mean 200 hPa geopotential height (Z200) in a CMIP and a set of AMIP simulations from the National Centers for Environmental Prediction (NCEP) Climate Forecast System Version 2 (CFSv2) are analyzed and compared with the NCEP/NCAR reanalysis. For the climate mean, it is found that a component of the bias in stationary waves characterized with wave trains emanating from the tropics into both the hemispheres can be attributed to the precipitation deficit over the Maritime continent. The lack of latent heating associated with the precipitation deficit may have served as the forcing of the wave trains. For the variability of the seasonal mean, both the CMIP and AMIP successfully simulated the geographical locations of the major centers of action, but the simulated intensity was generally weaker than that in the reanalysis, particularly for the center over the Davis Strait-southern Greenland area. It is also noted that the simulated action center over Aleutian Islands was southeastward shifted to some extent. The shift was likely caused by the eastward extension of the Pacific jet. Differences also existed between the CMIP and the AMIP simulations, with the center of actions over the Aleutian Islands stronger in the AMIP and the center over the Davis Strait-southern Greenland area stronger in the CMIP simulation. In the mode analysis, the El Nino-Southern Oscillation (ENSO) teleconnection pattern in each dataset was first removed from the data, and a rotated empirical orthogonal function (REOF) analysis was then applied to the residual. The purpose of this separation was to avoid possible mixing between the ENSO mode and those generated by the atmospheric internal dynamics. It was found that the simulated ENSO teleconnection patterns from both model runs well resembled that from the reanalysis, except for a small eastward shift. Based on the REOF modes of the residual data, six dominant modes of the reanalysis data had counterparts in each model simulation, though with different rankings in explained variance and some distortions in spatial structure. By evaluating the temporal coherency of the REOF modes between the reanalysis and the AMIP, it was found that the time series associated with the equatorially displaced North Atlantic Oscillation in the two datasets were significantly correlated, suggesting a potential predictability for this mode.

Keywords Model bias · Climate variability · Dominant modes of circulation · Predictability

1 Introduction

The second version of climate forecast system (CFSv2) of the National Centers for Environmental Prediction (NCEP) (Saha et al. 2014), with significant improvement in hindcast skills (Peng et al. 2013), was implemented for operational climate forecast in March 2011. Meanwhile, a series of diagnostics studies towards understanding various

---

This paper is a contribution to the Topical Collection on Climate Forecast System Version 2 (CFSv2). CFSv2 is a coupled global climate model and was implemented by National Centers for Environmental Prediction (NCEP) in seasonal forecasting operations in March 2011. This Topical Collection is coordinated by Jin Huang, Arun Kumar, Jim Kinter and Annarita Mariotti.

P. Peng (✉) · A. Kumar
Climate Prediction Center, NCWCP, NECP/NOAA, 5830 University Research Court, College Park, MD 20740, USA
e-mail: Peitao.Peng@noaa.gov

B. Jha
INNOVIM, LLC, Greenbelt, MD, USA

aspects of the model performance are being conducted. These studies are aimed at understanding and documenting model's simulation of climate variability, and more importantly, documenting model biases that could be targeted for improvement in future developmental efforts. As a part of the ongoing CFSv2 diagnostics effort, this study focuses on the comparison of seasonal mean atmospheric circulation in a fully coupled free run (CMIP-type) and a set of observed SST forced runs (AMIP-type) of the CFSv2, and also on the comparison of model results with that from the reanalysis data. These comparisons are expected to tell the impact of air-sea interactions and the realism of model performance in this respect. For the sake of brevity, the analysis presented here is for the Northern Hemisphere (NH) winter season (December–January–February) only. The reason for choosing the winter season is that for this season the circulation is more active than in other seasons due to the largest temperature contrast between the tropics and the polar region, and further, tropical-extratropical teleconnection related to ENSO SST variability is best defined (Newman and Sardeshmukh 1998).

Since many features of large scale circulation are well depicted by 200 hPa geopotential height (hereafter denoted by Z200), most analyses in this study is for the Z200 field. Following the time mean versus transient formalism of decomposing characteristics of circulation (Wallace and Blackmon 1983), this study examines the climate mean, variance and major modes of the December–January–February (DJF) seasonal mean Z200. In comparison with observations, the analysis documents how well the model can simulate the stationary waves, the distribution and amplitude of the DJF variability, and the spatial and temporal characteristics of the variability.

Since the pioneering work in the earlier 1980s by Wallace and Gutzler (1981) and Horel (1981), the mode analysis has become a common tool in climate diagnostics and modeling studies (Kang and Lau 1986; Mo and Livezey 1986; Barnston and Livezey 1987; Kushnir and Wallace 1989; Kumar et al. 2005). The mode analysis helps in understanding of the dynamics and predictability of climate phenomena, since different modes, with their unique spatial patterns and temporal characteristics, may owe their existence to different internal and external sources of variability. In the practice of extended-range weather and short term climate predictions, it is particularly important for a model to be able to generate modes of variability realistically so as to be able to correctly predict weather regimes and boundary forced climate anomalies.

In past, the empirical orthogonal function (EOF) technique, or its variant the rotated EOF (REOF), is usually applied to monthly or seasonal mean data to quantify major modes of climate variability. The procedure, although simple and efficient, has the potential to mix internal and external sources of variability. For example, the methodology can easily intermingle teleconnection pattern due to the El Nino-Southern Oscillation (ENSO) SST variability with the Pacific-North-America (PNA) pattern associated with internal atmospheric variability since the spatial signature of two patterns are quite similar over the PNA region. In order to avoid mixing two different sources of variability, Straus and Shukla (2002) grouped data into ENSO years and non-ENSO years and treated them separately in their analysis of dominant modes of variability. Their approach can distinguish ENSO related pattern of variability from the PNA pattern, but has two drawbacks: (a) the information of PNA pattern is not continuous in time, and (b) it is likely that PNA pattern also exist in ENSO years (Peng and Kumar 2005). In this study we follow an alternate approach: first remove the component of Z200 variability associated with ENSO pattern based on linear regression, we then apply the REOF analysis to the residual field. As the results will demonstrate, this approach is quite effective and efficient in separating internal and external modes of variability. Further, as the mode decomposition is done for all years, the procedure results in more complete temporal information for across both ENSO and non-ENSO years. This approach is particularly suitable to the analysis for a single time series of seasonal mean data, such as the reanalysis data and the CMIP-type run data where seasonal mean is comprised of both internal and external components of variability.

The paper is organized as follows: Sect. 2 provides a description of data used in the study and the analysis procedure. Section 3 presents the results of the analysis. Summary and discussions are given in the Sect. 4.

2 Data and analysis procedure

2.1 Data

The data used in this study include geopotential height at 200 hPa (Z200), wind at 200 hPa and surface (10 meter height), sea surface temperatures (SSTs), and precipitation rate (hereafter denoted by Prate). The model data are derived from two kinds of model simulations. One is a fully coupled free run (CMIP-type) with the full CFSv2, and the other is a set of model simulations forced with observed SSTs (AMIP-type) with the atmospheric component of CFSv2. Details about CFSv2 can be found in Kumar et al. (2012) and Saha et al. (2014).

The corresponding observational data is taken from the NCEP–NCAR reanalysis (Kalnay et al. 1996) for height and wind, the CPC precipitation analysis (CMAP) (Xie and Akin 1996) for Prate, and the Extended Reconstructed Sea

Surface Temperature dataset (ERSST.v3) (Smith et al. 2008) for SST. Hereafter we refer to these data sets as observations.

The CMIP-type run started from January 2001 and proceeded to the end of 2101. The CO_2 concentration in this run was prescribed to the observed until available (2010) and was projected to increase by 2 ppm per year after 2010. The data used for this analysis is from the 100-year period of 2002–2101, with the first year data not included to avoid issues related to initial model drift. More detailed description about the CMIP-type run can be found in Saha et al. (2014).

The AMIP simulations include an ensemble of 12 members that started with different initial conditions from the beginning of 1950 and proceeded to the end of 2010. Different initial conditions are taken from the days surrounding and including the 1st January 1950. All runs were forced with the observed SSTs. The CO_2 concentration in the model was specified from observations.

Considering the time period of the CMIP run is different from that of the AMIP and each type of runs contains different CO_2 concentration, and that our intent is not to analyze trends due to changes in atmospheric composition, all the data used for the analysis in this study was detrended with the linear least square method.

The DJF seasonal mean anomalies were calculated with respect to the climatology over the whole period of the data. The data length for the reanalysis is 63 years (1949–2011), while for the CMIP and AMIP, it is 100 years (2002–2101) and 61 years (1950–2010), respectively. The CMAP precipitation data is shorter and is only 31 years long (1979–2010).

2.2 Analysis procedure

The climate mean, and the standard deviation of the DJF seasonal mean SST are calculated for both observations and the CMIP simulation to first compare the realism of SST variability in the coupled simulation. Special attention was paid to the comparison of the spatial pattern associated with ENSO SST variability, which was obtained by regression of global SST with the Nino3.4 SST index. The Nino3.4 SST index is the SST averaged over the area of 130°W to 170° and 5°S to 5°N.

We next compared climate mean for Z200 and Prate. In this comparison, the model biases in the stationary waves (eddy part of Z200) and the zonally asymmetric Prate were examined. The purpose of analyzing the zonally asymmetric component was to assess if the bias in stationary waves can be explained by the corresponding bias in tropical diabatic heating. In other words, it is hypothesized that at least part of the bias in the stationary waves is forced by the bias in the zonally asymmetric tropical diabatic heating. Following the examination for climate mean, the standard deviation of Z200 is used to quantify the geographic distribution and amplitude of circulation variability. In addition, climate bias in upper level jets and their relationship with the bias in circulation variability was also examined. The reason for examining this relationship is that low-frequency variability is dynamically associated with the climatological jet streams (Branstator 1992). Therefore, to some extent a bias in low frequency variability could be related to the mean bias in jet streams.

The next step in our analysis was the mode decomposition for the Z200 variability. As mentioned before, this analysis was done in two steps. The first is to get the ENSO teleconnection pattern by regressing Z200 to the Nino34 index. Based on the yearly value for the DJF Nino 3.4 SST index, the corresponding linearly reconstructed Z200 was then removed from the data. We are aware of that the atmospheric responses to El Nino and La Nina are not exactly symmetric (Hoerling et al. 1997), and thus the linear ENSO removal may not be very clean, but considering the linear response is the dominant response, we keep in the framework of linear analysis. The second step was to find the leading modes of the NH circulation patterns by applying the rotated EOF (REOF) analysis to the residual. In order for the analysis of the AMIP-type ensemble simulations to mimic that for the observation and the CMIP run, 12 members of the AMIP runs were first concatenated into one long time series.

For ENSO teleconnection regression pattern, the Nino3.4 SST index from observation is used for the reanalysis and the AMIP data, while the index from the CMIP simulations was used for the CMIP run data. The spatial domain for the EOF analysis was from 20°N to 90°N so as to focus on patterns for middle and higher latitudes. For the variability at different latitudes to be treated equally, the data are weighted with the square root of the cosine of latitude. The EOF analysis is based on covariance matrix, so as to have more variance explained with fewer leading modes. The number of EOF modes kept for rotation is 10 for the observation and the CMIP run, and 12 for the AMIP run. These cutoff numbers were chosen for an optimal use of REOF (O'Lenic and Livezey 1988).

After the REOF analysis, common modes of the three datasets are identified and compared to each other. The rankings in explained variance, and the amplitude of the regression and correlation patterns, are used to compare the relative strength of these modes. Pattern correlations between the modes from model simulations and those from observations were computed for comparing the spatial structure.

We conclude the analysis with an assessment of SST forcing for different modes for AMIP simulations. This was done by evaluating temporal coherency between

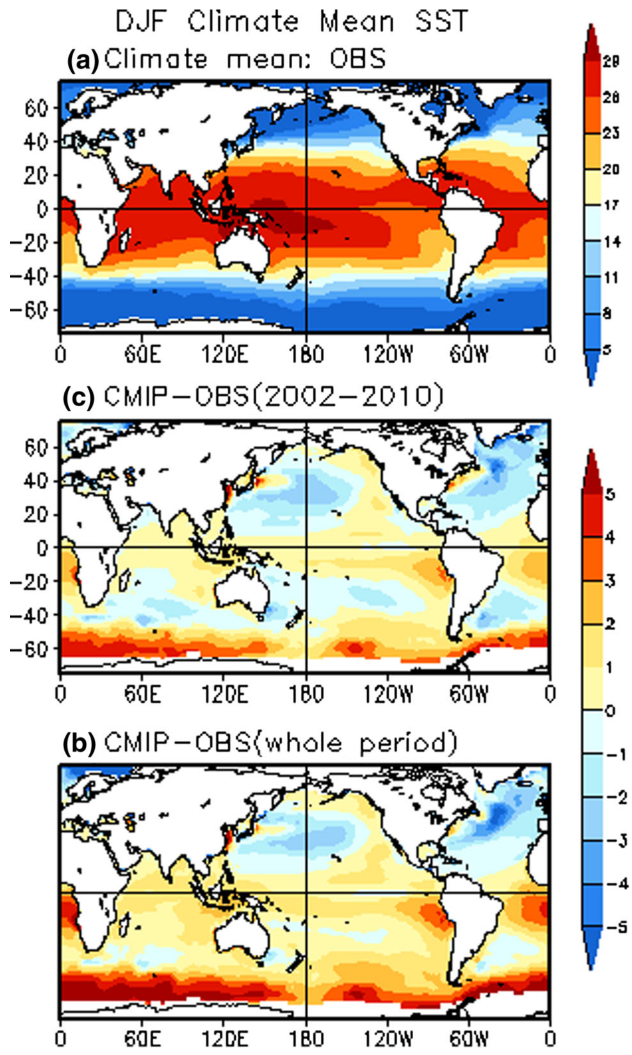

Fig. 1 Climate mean of DJF SST (°C): **a** climate mean of observation over the period of 1949–2011; **b** CMIP climate mean minus the observed over their common period of 2002–2010; **c** CMIP climate mean over 2002–2101 minus the observed over 1949–2011

modes from the AMIP simulation and their counterparts in observation. SST and surface wind patterns are identified with regression technique for understanding the coherent evolution between AMIP and observations.

3 Results

3.1 Model bias in SST

One of the basic assessments of coupled model simulations is the SST since biases in SSTs can influence atmospheric variability through air-sea interactions. Biases in SST simulations can be both in the mean climatology and its variability. Figure 1 shows the climate mean DJF SST for observation and the CMIP simulation, with the upper panel for observation over the period of 1949–2011, the middle panel for the deviation of the CMIP from the observation over the overlapping period of 2002–2010, which can be approximated as the mean bias of the model, and the lower panel also for a deviation for the CMIP simulation but with the data period being 1949–2011 for observation and 2002–2101 for the CMIP. A purpose for presenting the deviation in the lower panel is to examine the background state of the inter-annual variability over the whole period of the CMIP simulation.

The model mean bias shown in the middle panel, obtained as the model minus observed climatology over their overlapping period, is towards a warmer state in the tropical and southern high latitude oceans and colder state in northern and southern middle latitude oceans. Prominent warm bias is found in the tropical oceans off the west coasts of South America and Africa, and is due to the model errors in the estimate of marine stratus clouds over those regions (Xie et al. 2006; Huang et al. 2007; Hu et al. 2008). The same model errors are likely responsible for the warm bias in the southern oceans off the coast of Antarctic as well (Wanqiu Wang, personal communication). The lower panel exhibits enhanced warmer temperatures than that in the middle panel, with the warmer area extending to most southern oceans. The northern oceans, however, remain colder. The tendency towards a general warming in tropical and southern oceans is consistent with the warming SST trend in the CMIP run (not shown), and therefore, may be attributed to the imposed, and increasing, CO_2 forcing. As no corresponding cooling trend is found in the CMIP run for the northern oceans (Jha et al. 2013), the cold bias there can't be simply attributed to the CO_2 forcing. The zonally asymmetric component of the SST bias (that would tend to downplay the tendency towards warmer SSTs) is also in good agreement with the SST bias in short range initialized predictions (Kumar et al. 2012; Xue et al. 2013) confirming that the cold bias is unrelated to an increase in CO_2.

Figure 2 shows the standard deviation of DJF SST, with the upper panel for the observation over the period of 1949–2011, and lower panel for the CMIP bias, that is, the CMIP minus observation. The CMIP variability is based on its 100 year data (2002–210). For the observation, the maximum in the eastern and central equatorial Pacific is due to the SST variability related to ENSO. The local maximum in middle and higher latitudes is because of active atmospheric forcing (i.e. wind driven) related to the mid-latitude storm track over those regions (Frankignoul 1985). Further, a part of the SST variability in North Pacific is also due to response to ENSO teleconnections (Wang et al. 2012). In the CMIP bias shown in the lower panel, there is a modest positive bias in the equatorial Pacific, indicating stronger ENSO variability in the model.

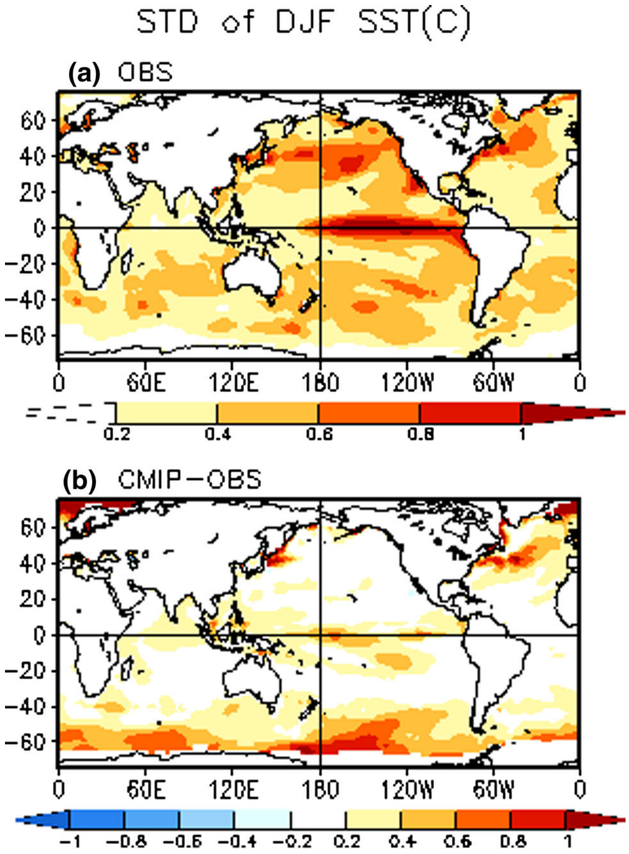

Fig. 2 Standard deviation of DJF SST (°C): **a** observation; **b** CMIP minus the observation. The data periods are 1949–2011 for the observation and 2002–2101 for the CMIP. All data are linearly detrended

Other regions with positive bias in the SST variability exist over North Atlantic and the southern oceans near the Antarctic. Over all, the inter-annual variability of DJF SSTs in the CMIP run is comparable to that in observation.

The most important inter-annual variability in SST is associated with ENSO. In order to describe the ENSO behavior in free coupled simulations, Saha et al. (2014) computed the power spectrum of Nino34 SST index in the CMIP simulation, and found a spectral peak over 0.2–0.3 cycles per year frequency band, narrower than that in observations (0.15–0.45 cycles per year). A narrower spectrum band means more regular ENSO occurrence in the CMIP run. Here we present the ENSO related SST pattern in the model and compare it with that from observation. Figure 3 shows the spatial pattern of global SST regression to the Nino34 SST index for observation and for the CMIP simulation. It can be seen that the model pattern resembles the observation very well, and some differences are (1) larger amplitude for ENSO related SSTs in the tropical Pacific consistent with the larger interannual standard deviation (Fig. 2), and (2) a larger meridional width of ENSO related signal in the equatorial tropical Pacific.

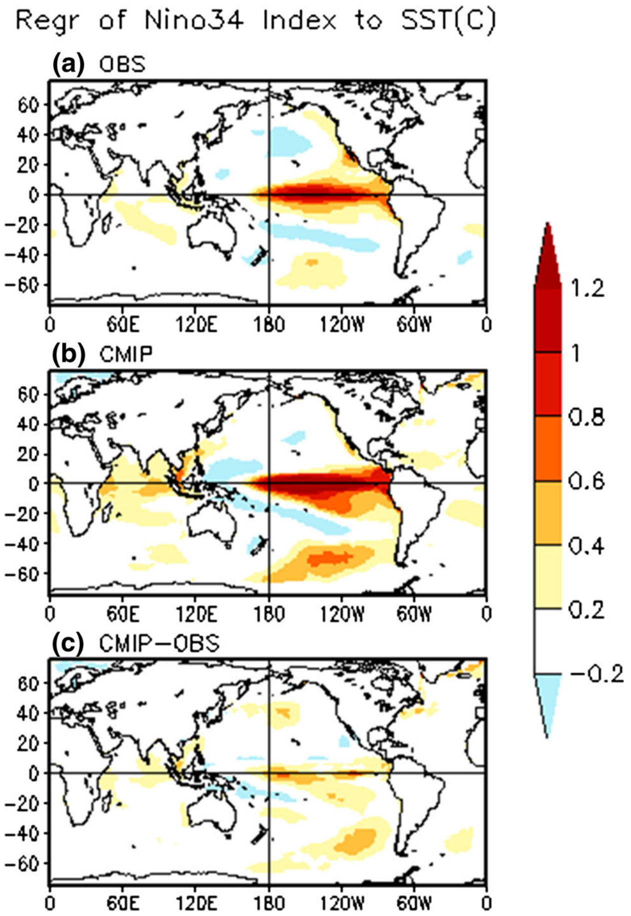

Fig. 3 Regression of global SST (°C) to the Nino3.4 SST index for DJF season: **a** from observational data over 1949–2011, **b** from CMIP data over 2002–2101, and **c** the result of **b** minus **a**. All the data are linearly detrended

3.2 Model bias in climate mean precipitation rate (Prate) and stationary waves

Atmospheric stationary waves determine the zonally asymmetric distribution of other features of climate, for example, surface temperature and precipitation. The stationary waves owe their origin to asymmetric distribution of tropical heating, surface orography, transient fluxes associated with momentum etc. (Nigam et al. 1986, 1988; Held et al. 2002). Biases in the model representation of these forcings may also cause bias in the simulation of stationary waves. Considering precipitation (Prate) as a measure of the vertically integrated condensational heating, which is one of the major forcings for the general circulation, here we examine, and relate, model bias in Prate with the stationary wave bias.

Figure 4 presents the climatology of zonally asymmetric Prate (left column) and eddy Z200 (right column), representing stationary waves for observation, CMIP and AMIP simulations. The reason for removing the zonally symmetric

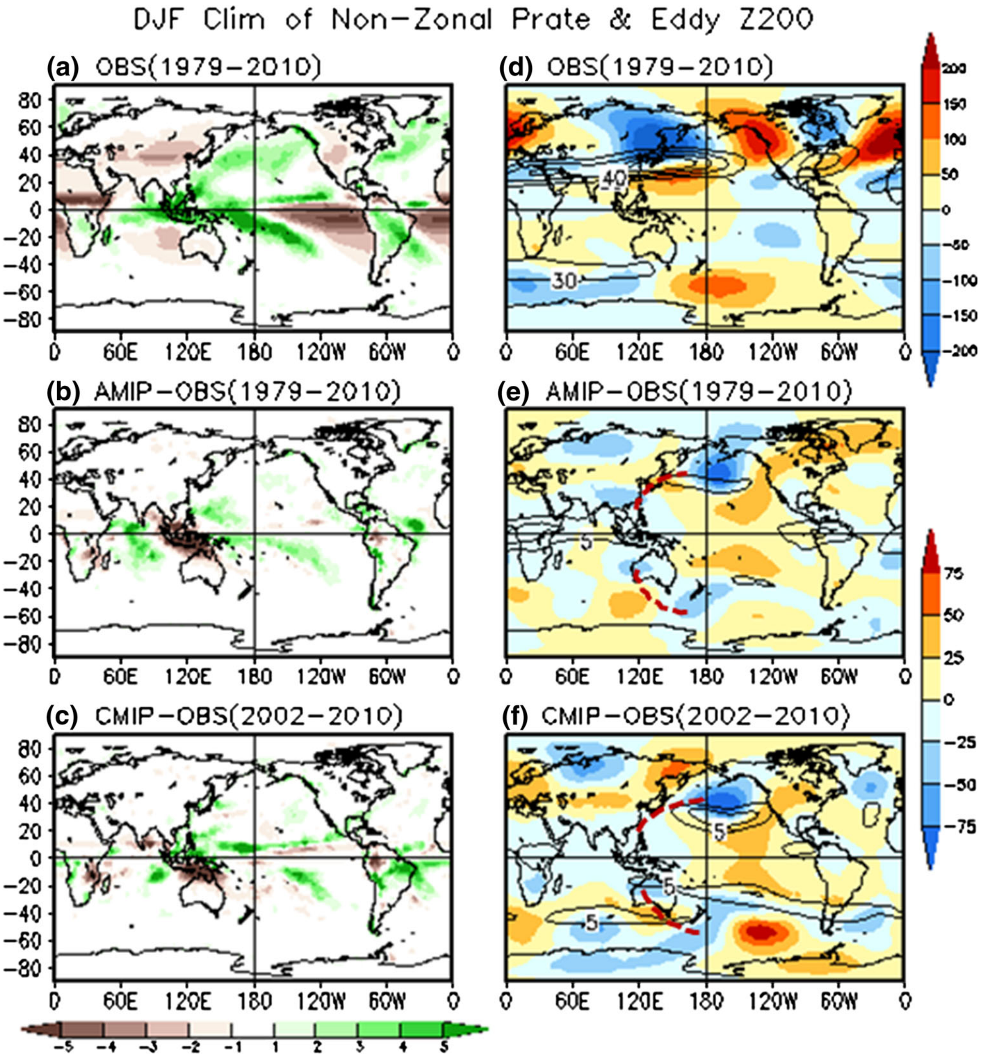

Fig. 4 Climate mean of the zonally asymmetric DJF precipitation rate (mm/day) (*left column*) and eddy 200 hPa height (m) (*right column*): The *upper row* is for the climate of observation over 1979–2010, the *middle row* is for the bias of AMIP runs from the observation over the same period, and the *bottom row* is for the bias of CMIP run over 2002–2010. The contours with the height fields are the climate mean of 200-mb zonal wind (U200) in observation (**d**) and model bias for AMIP and CMIP runs (**e**, **f**). With m/s unit, the contour levels for U200 climate are 30, 40, 50 and 60, for U200 bias are 5, 10, and 15. The *red dotted lines* illustrate the paths of anomalous stationary wave trains from the tropics

part of the Prate is to provide a more direct connection with eddy Z200. The upper panels of the figure are for observations, while the middle and lower panels are for the bias in AMIP and CMIP simulations, respectively. The time period over which climatology is calculated is 1979–2010 for the observation and AMIP simulations because satellite retrieved precipitation data are available only since 1979. For the sake of a fair comparison, the bias of the CMIP run is calculated with the data over 2002–2010, the overlapping period of the observation and the CMIP run.

In Fig. 4a positive values of Prate in tropics are associated with the strong convection over the Indo-Pacific warm pool area, and over the South America, and also in association with the South Pacific Convergence Zone (SPCZ) and the Intertropical Convergence Zones (ITCZs) in equatorial Pacific and Atlantic oceans. In contrast, the negative values of Prate (i.e., values below the zonal mean average) are over relatively cooler SST regions, including the eastern tropical South Pacific and South Atlantic oceans, and also over the semi-arid regions of Africa. In the extratropics, positive Prate is associated with the location of storm tracks over the two ocean basins, and the negative Prate values are found over the Asia and the North American lands. Comparing Fig. 4a, d, we can see that there is a good agreement between the positive values of Prate in tropics and the subtropical Z200 with pairs of highs in the subtropics (corresponding to anticyclones) straddling major positive Prate regions and pairs of subtropical lows (corresponding to cyclones) straddling major negative Prate regions. These subtropical anticyclone (cyclone) pairs, seen as a part of stationary waves, can be explained as the Rossby wave responses to the zonally asymmetric diabatic heating (cooling) (Gill 1982). In addition, in Fig. 4d we also show climate mean zonal wind at 200 hPa (U200) with contours to locate the jet streams. The geostrophic relationship between the jet and the meridional gradient of Z200 is obvious in the figure.

Having examined the relationship between climatological spatial tropical heating and stationary waves in observation, we turn our attention to model bias. Figure 4b, c show the model bias in Prate for the AMIP run and the CMIP simulations, respectively. It is found that the largest Prate bias for the two types of runs is in tropics. This is to be expected since the largest values for Prate are also located in tropical latitudes, and larger biases can be associated with large mean. The spatial patterns of bias for two simulations is very similar with a strong deficit over the Maritime continent over the western Pacific and regions with positive rainfall bias spread over the other three ocean basins.

Consistent with the similarity between precipitation bias, model bias in stationary waves for the two simulations (Fig. 4e, f) also show similar patterns, with lows (highs) over the Prate deficit (surplus) areas in the tropics and wave-like features in the extratropics. A careful examination on the features of the stationary wave bias over the globe reveals a pair of wave-trains emanating from the area over the Maritime continent and spreading to the middle and higher latitudes of both hemispheres. The wave-train feature of the bias is particularly evident in AMIP run (Fig. 4e). The pair of the wave trains is symmetric about the equator, with the Northern Hemisphere branch being stronger and resembling the PNA pattern. The phase structure of these wave trains is found to be qualitatively similar to the linear model response to the diabatic cooling in western Pacific (Peng 1995; DeWeaver and Nigam 2004), therefore, we conjecture that the wave-train-like bias in stationary wave is caused (or forced) by the latent heat deficit over the Maritime continent in the western Pacific. In general, the tropically forced wave train is in essence a Rossby wave, with its vertical structure being baroclinic in the tropics and barotropic in the extratropics (Ting 1996), and extending along the great circle around the globe (Hoskins et al. 1983).

The model bias in U200 is shown with contours in Fig. 4e, f. It is found that in both simulations, the Pacific jet is enhanced and shifted eastward. Comparing the U200 bias with the Z200 bias, one can easily see the geostrophic relationship between the two. In fact, the zonally asymmetric part of U200 bias, which is dominant, must be a manifestation of stationary wave bias in Z200 field.

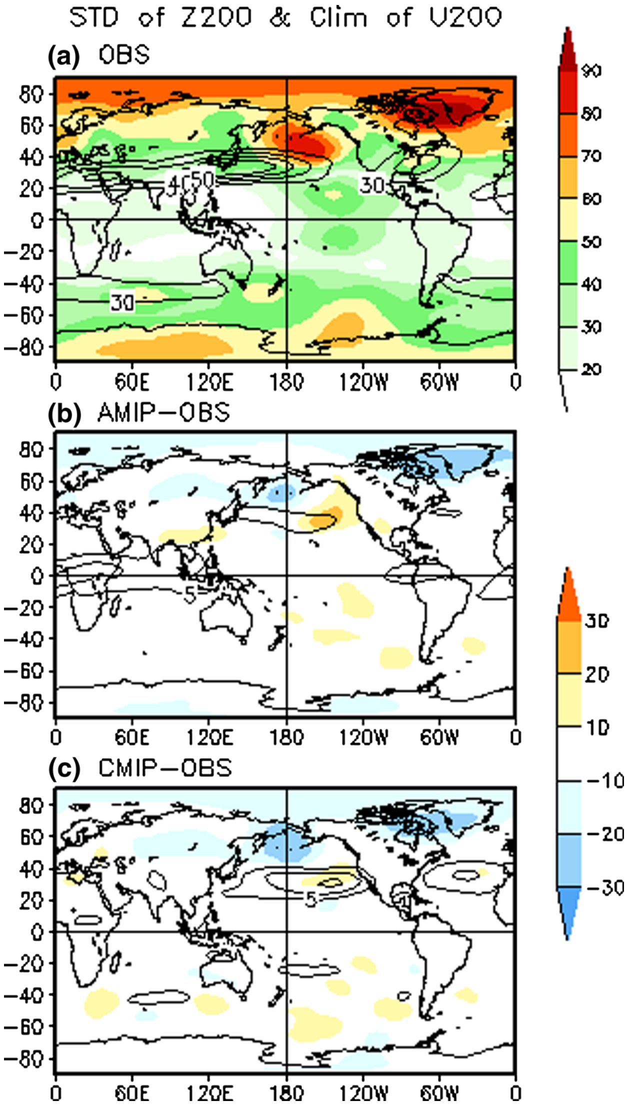

Fig. 5 Standard deviation of DJF mean Z200 (m): **a** total quantity of the observation; **b** AMIP minus observation; **c** CMIP minus observation. The contours, with the same levels and unit as that in Fig. 4, are for the corresponding climate mean U200. The results are based on the data from the whole period of each dataset

3.3 Model bias in Z200 variability

In this section, we examine the model bias in the interannual variability of DJF mean Z200. Shown in Fig. 5 is the standard deviation of Z200, with the upper panel showing for the observation, and the middle and lower panels the bias for the AMIP and CMIP model simulations. All the results are based on the data over the entire period of the respective datasets. For the Z200 variability in observation (Fig. 5a), the most noticeable features are the four local maxima (or called centers of action), two of them are in the NH extratropics and the other two are in the subtropics. In the NH extratropics, one center is over the North Pacific located south of the Aleutian Islands. The other one, also the stronger of the two, is over the North Atlantic sector, over the Davis Strait-Southern Greenland region. We will see later that the both centers are associated with some dominant mode of climate variability, such as the ENSO teleconnection and PNA patterns over Pacific, and the North

Fig. 6 Regression patterns of DJF mean precipitation rate (mm/day) (*left column*) and 200 hPa height (m) (*right column*) to the Nino3.4 SST index for observation (*top row*), AMIP data (*middle row*), and CMIP data (*bottom row*). For the height patterns, the contours are for regression and shading for correlation, with contour interval of 10 m, and *shaded areas* passing the 95 % significant level. The data periods are the same as that in Fig. 5

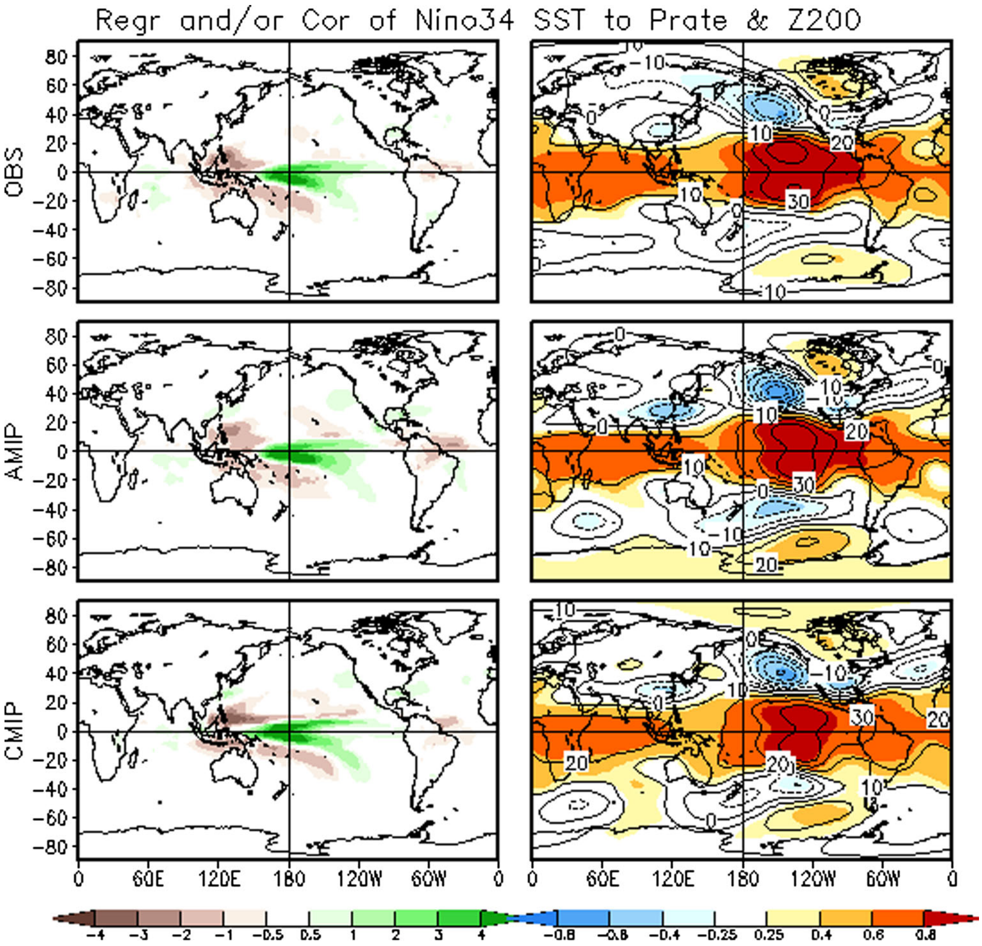

Atlantic Oscillation (NAO) pattern over northern Atlantic. The two subtropical centers are in the eastern Pacific and are symmetric about the equator, and as will be discussed later, are associated with ENSO teleconnection patterns.

For the model bias in Z200 variability (Fig. 5b, c), the both centers of action in NH extratropics are weaker than in observation. In particular, the center over the North Atlantic is about 30 % weaker in amplitude in both simulations. This bias is quite common across a range of climate models. For the North Pacific center, the bias is not only in strength, but also in the location. The center of variability is south-eastward shift with respect to the observed. Comparing the two simulations, one can see that the amplitude bias is less for the AMIP, but south-eastward shift in its location is more profound.

As in Fig. 4, the observed U200 climatology and the bias in model simulations are also shown in Fig. 5. The U200 bias for CMIP run here (Fig. 5c) is stronger and more eastward extended than that in Fig. 4f. The reason is that the U200 climatology of CMIP used here is taken over the whole 100-year period, reflecting the response to the projected CO_2 forcing.

3.4 ENSO patterns in Prate and Z200

We next examine the dominant modes of NH DJF circulation. As mentioned before, in the methodology adopted for the mode decomposition of this study, ENSO-related pattern is first linearly removed, and then other patterns of variability are computed from the residual.

Figure 6 shows the Prate (left column) and Z200 (right column) patterns associated with ENSO for observation and model simulations, and are obtained as regressions/correlations with the Nino34 SST index. The purpose of showing ENSO regression for Prate is to assess the ENSO related tropical heating, which serves as the direct forcing for the corresponding global teleconnection pattern. Both the Prate and Z200 patterns have appeared previously in literature and their dynamics have also been extensively studied (see Trenberth et al. 1998; Hoerling and Kumar 2002 and references there in). Our interest here is to compare the model results with observation.

For Prate, the results for simulations are in good agreement with observations both in spatial structure and for amplitude. Although the amplitude of ENSO SST pattern in the CMIP is somewhat larger than in observation over the central and eastern equatorial Pacific (see Fig. 3c), the differences in Prate related to ENSO are small. The results for the ENSO regression pattern for Z200 (in contours) are also encouraging with pattern correlation coefficients between model and observation exceeding 0.92. However, a more careful analysis reveals some biases in the geographical locations of the high and low centers over the Pacific, and the model simulated subtropical highs are eastward shifted with respect to the observed. Similar shift also appears in the center of low in the North Pacific, but with a little bit southward component added. The shift of the pattern is likely due to the eastward extension of the climatological Pacific jet as shown in Figs. 4 and 5. The eastward extended jet, along with the extended storm track, could lead to an eastward shift in the ENSO pattern through the forced wave-basic flow interaction and also transient eddy forcing (Sardeshmukh and Hoskins 1988; Held et al. 1989 and Ting and Sardeshmukh 1993). This possibility is also supported by the comparison of the CMIP and AMIP and the extent of pattern shift and jet extension. The pattern shift in the CMIP is more apparent than that in the AMIP, and thus is consistent with the more extended jet in the CMIP simulation. We also noted that in the observation, the North Pacific low in the pattern has its tail extending to north Asia, while in the model the extent of low is confined to that over the ocean. In addition, the AMIP has stronger response in North Pacific, and partially accounts for its stronger variability than for the CMIP run over that area (see Fig. 5). As to why the ENSO pattern in the AMIP run is stronger than that in the CMIP is not apparent as their tropical heating is almost the same. The difference may be in basic state or/and in the amplitude of transient eddy forcing.

The relationship between Z200 and Nino34 SST index is also quantified by correlations, which are depicted with shadings in the three right panels of Fig. 6. The colored shadings are applied to the areas with the absolute values of the correlation coefficients exceeding 0.25. The number 0.25 is significant at 95 % level based on the *t* test for degrees of freedom 60. Because even the shortest dataset in this analysis, the AMIP simulation, is longer than 60 years and interannual variability is dominant in DJF Z200, the colored patterns in the right panels at least meet the 95 % significance level. As expected, high correlations are found in tropics. Beyond tropics, only moderate correlations appear in the crests and nadirs of the wave-like teleconnection patterns. The ENSO impact on the global Z200 variability can be better quantified by the fraction of total variance explained by ENSO. The variance fraction, shown in Fig. 7, is calculated by squaring the correlation coefficients between Nino34 and Z200 shown in Fig. 6. The color levels start from 6.25 %, which corresponds to the correlation coefficient of 0.25 and exceeds 95 % significance level based on *t* test. It is evident that ENSO accounts for a substantial fraction (30–80 %) of Z200 variance in tropics, but much less beyond 20° north and south. Comparing the three panels in Fig. 7, we can see that in tropics ENSO impact in observation is bigger than that in model simulations, while beyond tropics the impact in model simulations is bigger. The comparison also shows that the impact in the AMIP is bigger than that in the CMIP. Whether this difference is due to air-sea interaction or the projected CO_2 forcing is not clear.

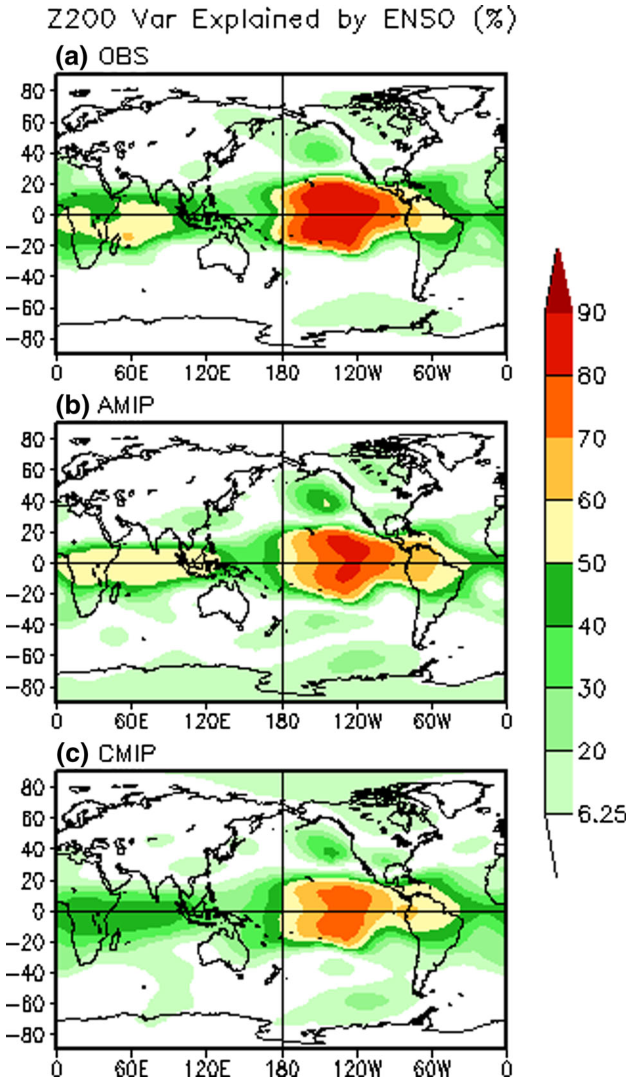

Fig. 7 Percentage of the variance of DJF Z200 explained by ENSO for the observation (**a**), the AMIP runs (**b**) and the CMIP run (**c**). The *shaded area* are above the 95 % significant level. The data perios are the same as that in Fig. 5

3.5 REOF modes of Z200 residual

In this section, we present the spatial patterns of six REOF modes of DJF Z200 for the observation and two model

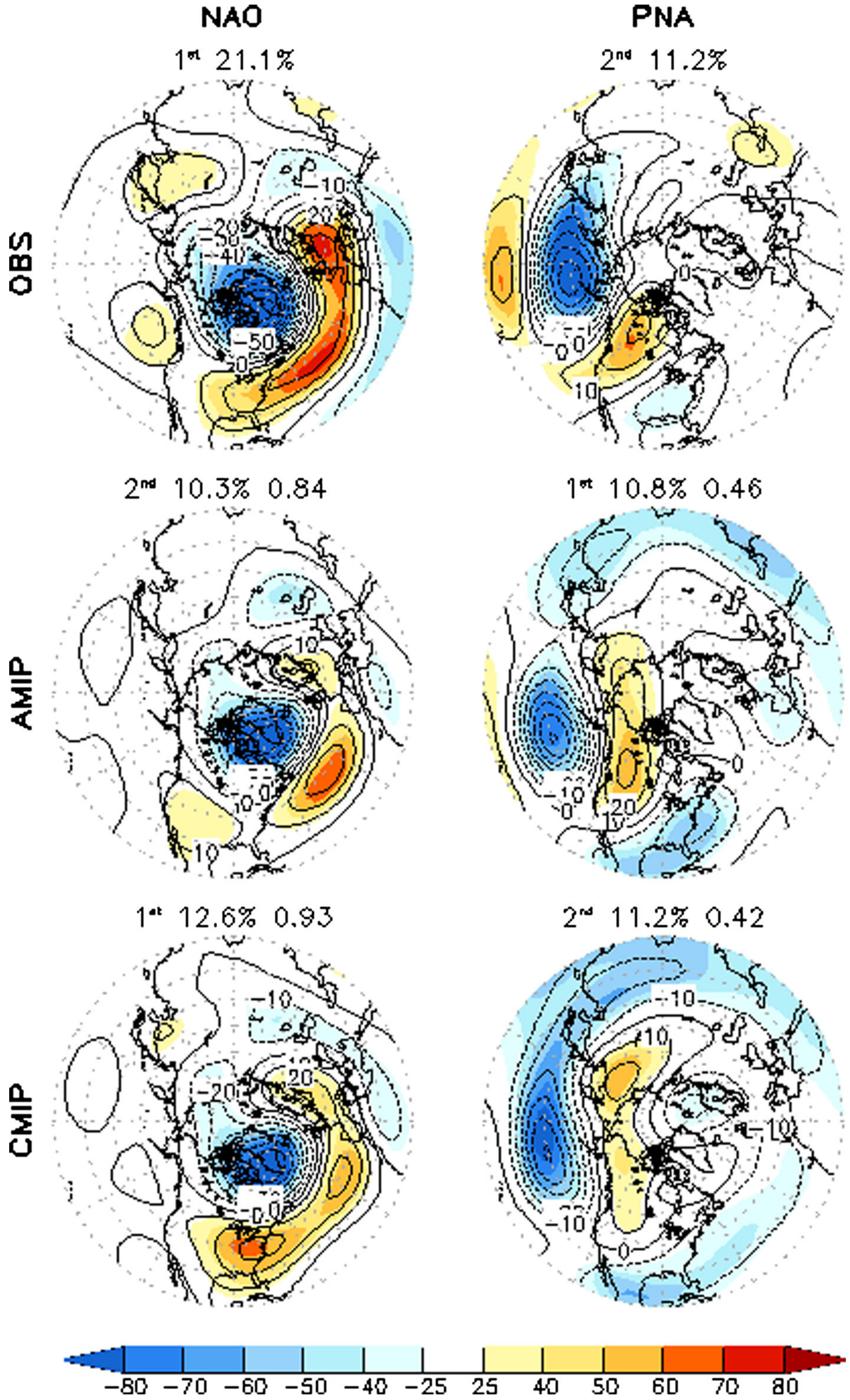

Fig. 8 NAO (*left column*) and PNA (*right column*) patterns of DJF Z200 for the observation (*top row*), AMIP runs (*middle row*) and CMIP run (*bottom row*). The patterns are obtained by regressing/correlating Z200 to the rotated principal components (RPCs) of the Z200 residuals (with ENSO related variability removed) over the extratropical Northern Hemisphere (20 N–90 N). The contours with interval of 10 m are for regression, and shading (%) for correlation. On the top of each penal, the numbers give the ranking, explained variance (%), and the spatial correlation between the pattern from model and that from observation, respectively

simulations. As mentioned before, the EOF analyses are performed with the Z200 residuals (i.e., with ENSO related variability removed) and over the spatial domain of 20 N–90 N. These six modes are selected because they exist in all three datasets. The patterns shown in the Figs. 8, 9 and 10 consist of two aspects, one is the regressions of Z200 to the normalized rotated principal component (RPC) time-series, and the other one is the correlation coefficients of Z200 to the RPCs. The regression patterns tell the relative strength of the modes, while the correlation patterns give

Fig. 9 As in Fig. 8, but for WPO and NA patterns

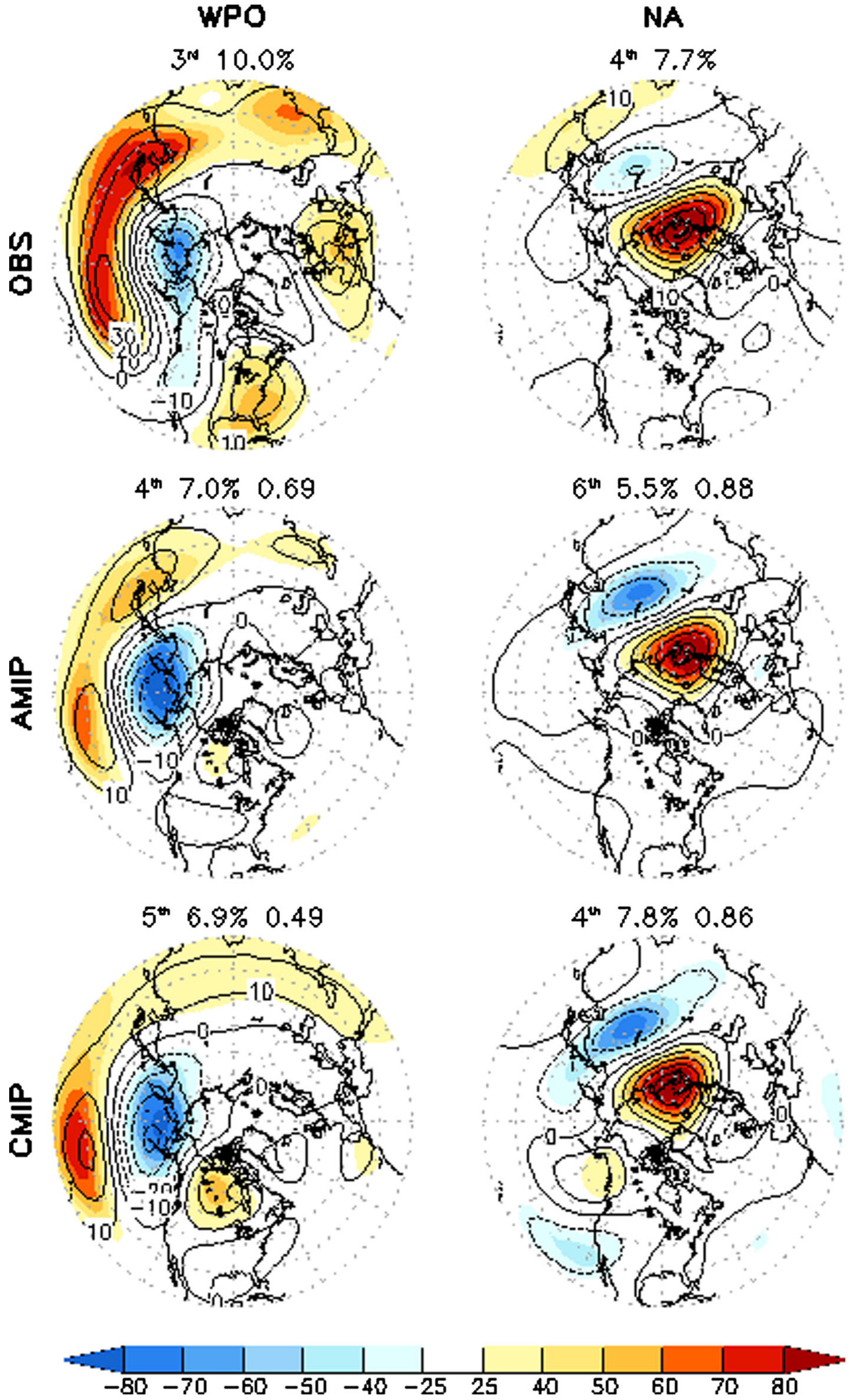

the information about the statistical significance of the pattern, and furthermore, squared correlation coefficients tell the fractions of local variance explained by the modes. Note the Z200 used in the calculation of the correlation patterns are total fields, not residuals, so correlations reflect the relative importance of the modes for the total variability.

Figure 8 shows the North Atlantic Oscillation (NAO) pattern (left column) and the Pacific and North America (PNA) pattern (right column) for the observation (upper),

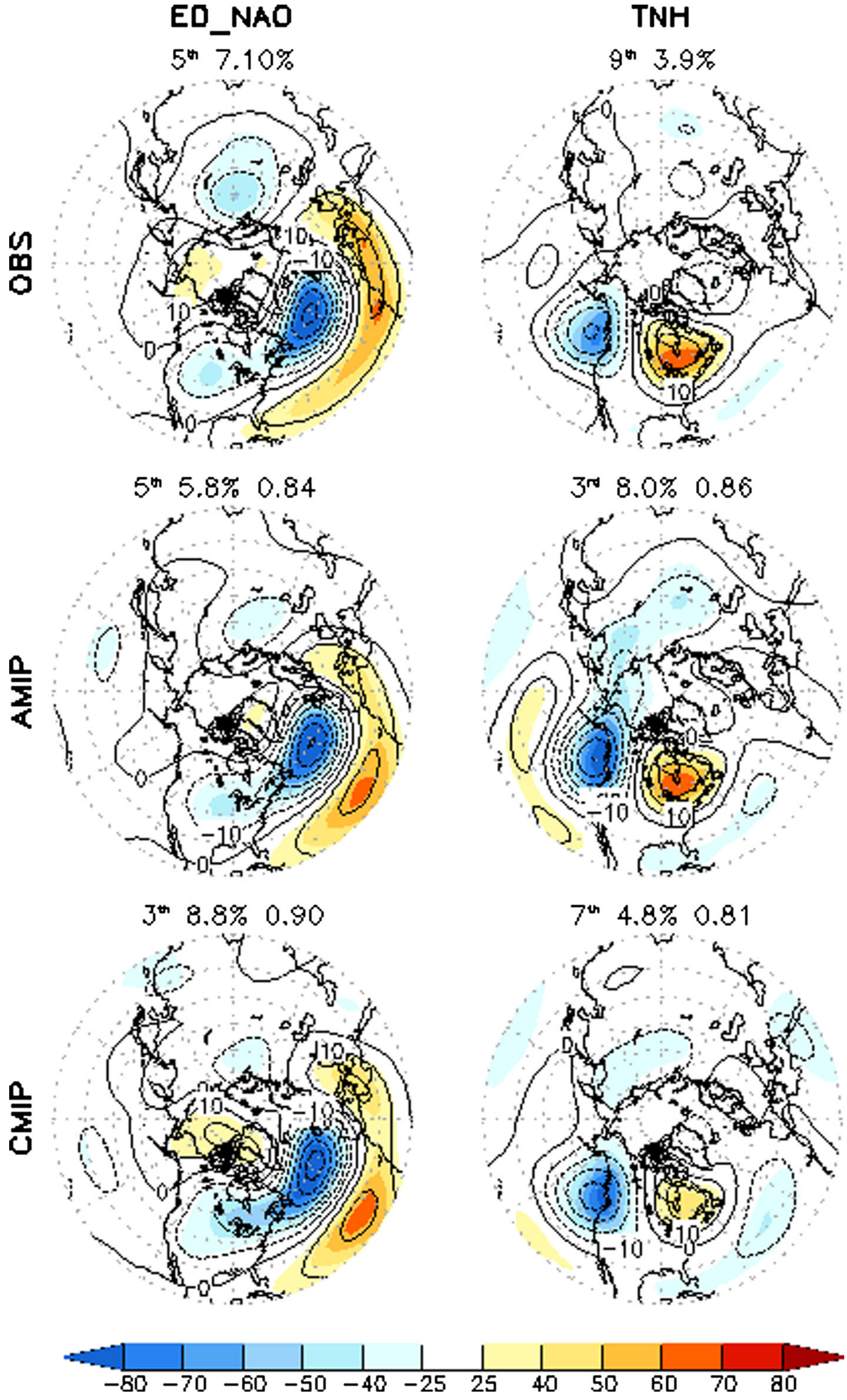

Fig. 10 As in Fig. 8, but for ED_NAO and TNH patterns AMIP (middle) and CMIP (lower). The numbers on the top of each pattern map are the ranking of the mode in explained variance and the quantity (%) of explained variance. For model simulated patterns, an additional number shown there is the pattern correlation between the observation and the model for the NH domain (20°N–90°N). In the maps, contours are for regression patterns and shadings for correlation patterns. Same as in Fig. 6, the color shadings indicate the 95 % and higher significance levels for the degrees of freedom 60.

The NAO pattern is the leading mode of variability in the observation and the CMIP run, but is the fourth mode in the AMIP run. The resemblance of the pattern in the CMIP to that in the observation is almost perfect, with correlation coefficient reaching 0.93. The correlation for the pattern with the AMIP is slightly lower ($r = 0.84$), due to some discrepancies over North Pacific.

The PNA pattern is the second leading mode in the observation and the CMIP run, but the first mode in the AMIP run. It is a dominant mode over the PNA region, and is associated with the zonal oscillation of the Pacific jet. This mode is very important in modulating the weather and climate of North America. The pattern from the AMIP is very close to that from the CMIP run, except the former is stronger. Comparing them with that from the observation, we can see the center of low over the North Pacific in the model simulations is southeastward shifted, and this bias is similar to that for the corresponding ENSO regression pattern. The shift is likely due to the eastward extension of the Pacific jet in the model. Differences are also found downstream to the center of low over the Pacific. As a result, their pattern correlations to that from the observation are below 0.5.

Figure 9 shows the west Pacific oscillation (WPO) pattern (left column) and North Asia (NA) pattern (right column). The WPO pattern is ranked third in the observation, second in the AMIP and fifth in the CMIP simulation. This mode is associated with the meridional oscillation of the Pacific jet (Linkin and Nigam 2008), with a downstream influence to North America. The patterns from the model runs are very alike to their observational counterpart; however, a southward shift with respect to that in the observation is apparent. The model-observation correlation for this pattern is 0.69 for the AMIP and 0.49 for the CMIP.

The North Asia (NA) pattern is the fourth mode in both observation and the CMIP, but the eighth mode in the AMIP simulation. The resemblance between the model results and that from reanalysis is strikingly high, with the pattern correlation 0.88 for the AMIP run and 0.86 for the CMIP run.

In Fig. 10, the pattern ranked fifth in the observation is similar to NAO in spatial structure, except it is equatorially displaced by about 20 degrees. This pattern is named the eastern Atlantic (EA) pattern in Wallace and Gutzler (1981), but we prefer to follow the nomenclature of van den Dool et al. (2006), and call it the equatorially displaced NAO (ED_NAO) because of its striking resemblance to the NAO. The ED_NAO pattern is the fifth mode in the AMIP and the third mode in the CMIP. Model simulations for this pattern are very close to observations both in their amplitude and pattern structure, with pattern correlations to the observation reaching 0.84 for the AMIP and 0.90 for the CMIP simulation.

The final pattern (right column of Fig. 10) in the comparison is the Tropical Northern Hemisphere (TNH) pattern (Mo and Livezey 1986) and is ranked ninth in observation, third in the AMIP and the seventh in the CMIP. The TNH pattern appears as a shifted PNA pattern, with the center of low close to the west coast of Canada. Model simulations for this mode are quite good, with pattern correlation coefficient with observation being 0.81 for the CMIP and 0.86 for the AMIP.

Based on the mode analysis, it is found that the six out of ten REOF modes in observation can be generated by CFSv2 in either the CMIP or the AMIP simulation, and four out of the six simulated modes have high pattern correlations to their counterparts in observation. The two modes (PNA and WPO) with lower pattern correlation are associated with the oscillations of the Pacific jet. Thus, it is conceivable that the bias in PNA and WPO modes is likely a result of the bias in the Pacific jet and its associated storm track. It is also evident that each pair of the patterns from two types of simulation is strikingly similar to each other. Because the two types of runs share the same atmospheric model, and have very close stationary waves, the striking similarity between the two runs suggests that these modes are intrinsic to the atmospheric variability, and the impact from the coupled air-sea interactions may not be very important. In addition, although some modes can only explain quite small fraction of the total variance over the entire NH domain, their explained local variance are generally much larger. This can be seen from locally large values of their correlation patterns.

3.6 Influence of SST to the REOF modes

After the examination of the six REOF modes from the Z200 residuals, a question is the possible influence of SSTs on these modes in the AMIP simulation. This is important in the context of the predictability of second kind, that is, the influence of boundary forcing. Since the AMIP runs are forced with the observed SSTs, for a particular mode to be influenced by SSTs it must demonstrate temporal coherence with its observational counterpart. The temporal coherency is quantified by correlation between the RPCs of a mode in the model and the corresponding mode in observation. The correlation actually gives the potential prediction skill of the mode if one can predict SSTs. We do the analysis based on ensemble average of 12 simulations to enhance signal–noise ratio by reducing the influence of internal variability (Kumar and Hoerling 2000). Based on this analysis we find that out of six modes, only the ED_NAO mode has its correlation (=0.44) exceeding the 99 % significance level based on t test with degrees of freedom 60. The other five modes in the model are not significantly influenced by the prescribed SST forcing, and

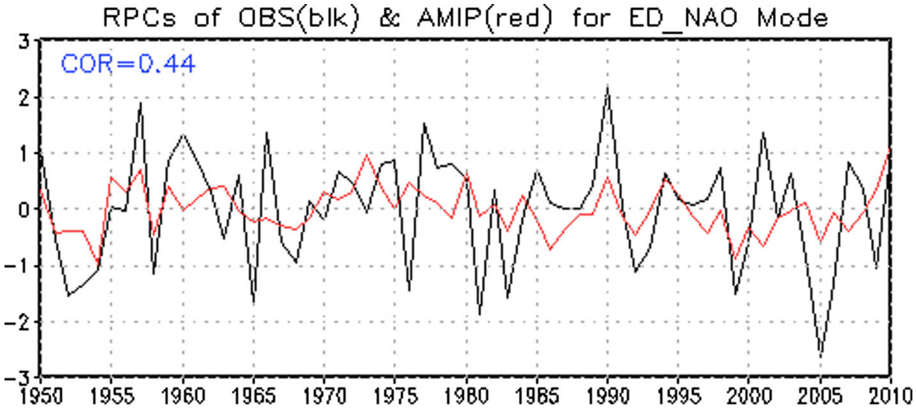

Fig. 11 Rotated principal components (RPCs) of the ED_NAO mode for observation (*black*) and the AMIP run (*red*). The RPC for observation is normalized, and so is the original RPC of the AMIP run. Shown here the RPC for the AMIP run is the ensemble mean of the 12 members. COR = 0.44 is the correlation between the two. With the degrees of freedom around 60, this correlation exceeds the 99 % significant level (0.33) in *t* test. The vertical axis is in the unit of standard deviation of the original RPCs

therefore, are dominated by atmospheric internal variability.

Figure 11 shows the RPCs of the ED_NAO mode for observation and the AMIP run. The original RPCs are normalized. The amplitude for the AMIP run has smaller amplitude, and is due to the noise reduction by the ensemble averaging. It turns out that the variance of the ensemble averaged RPC is about 20 % of the not averaged. It means the SST forced part accounts for about 20 % variance of the original variability in the ED_NAO mode for the model. This variance partition can be easily converted to a quantity of signal-to-noise ratio (SNR), which is defined as the ratio of standard deviation of ensemble mean over ensemble spread in the context of ensemble forecast. The obtained SNR for the ED_NAO mode is about 0.5. Visually the dominant variability of the RPCs is on inter-annual time scale. This is confirmed by their auto correlations, with 1-year lag value being 0.25 for the AMIP run and 0.002 for observation.

Considering the RPCs are calculated from residuals, one may question the influence of the ENSO removal to the results. In order to clarify this, we generate two time series by projecting the ED_NAO pattern onto the Z200 total fields and residuals respectively, then compare them each other and with the corresponding RPC. Figure 12 shows the results from the observational data. Evidently the two time series from projections (black and red lines) are almost identical, with temporal correlation coefficient over the 63-year period about 0.99. This is to be expected because as shown in Fig. 7, the ENSO explained variance over the extratropical Atlantic is small. The differences between the projection generated time series and the RPC (blue line), however, are more identifiable with temporal correlation around 0.9. This discrepancy comes from the non-orthogonality of REOF patterns, which makes the RPCs-to-patterns calculation not exactly reversible.

In order to identify and understand the SST forcing responsible for ED_NAO mode in the AMIP simulation, we calculated correlations of SST to the RPCs shown in Fig. 11. The SST correlation patterns, together with the patterns of regression of surface wind (at 10 m height) and Z200 to the same RPCs, are displayed in Fig. 13 for observation and the AMIP run. The AMIP data of wind and Z200 used in the regression calculation are ensemble averages of the 12 members. In observation (left panel), the most prominent SST feature is the negative anomaly to the south of the low. Because the wind over this area is stronger-than-normal westerly (i.e., positive wind anomaly associated with the ED_NAO pattern), the negative SST anomaly is likely caused by the southward Ekman transport (Kushnir et al. 2002), and also forced by local atmospheric heat fluxes resulting from the mean wind anomaly and high frequency weather associated with the ED_NAO pattern. According to Fan and Schneider (2012), high frequency weather is dominant in generating heat flux forcing. Therefore, the SST anomaly corresponding to the ED_NAO pattern in observation is primarily wind-driven. By comparing the SST correlations in the AMIP run, it is found that the SST pattern is almost the same as that in observation, except the correlation value is lower. That the SST forcing for this mode in the model has the same pattern as the wind-driven SST in observation means that a part of the ED_NAO mode in model is indeed forced by the SST that in observations is also driven by this pattern. This analysis suggests that in observation there may exit SST feedback for the ED_NAO mode, and the SST feedback could make the life span of this mode longer (Peña et al. 2004). The reason that SST correlation is not higher in the AMIP run is that not all the observed SST variability over the region shown in Fig. 13 is driven by the ED_NAO pattern, and further, feedback of SSTs on constraining atmospheric variability is weak (Bretherton and Battisti 2000).

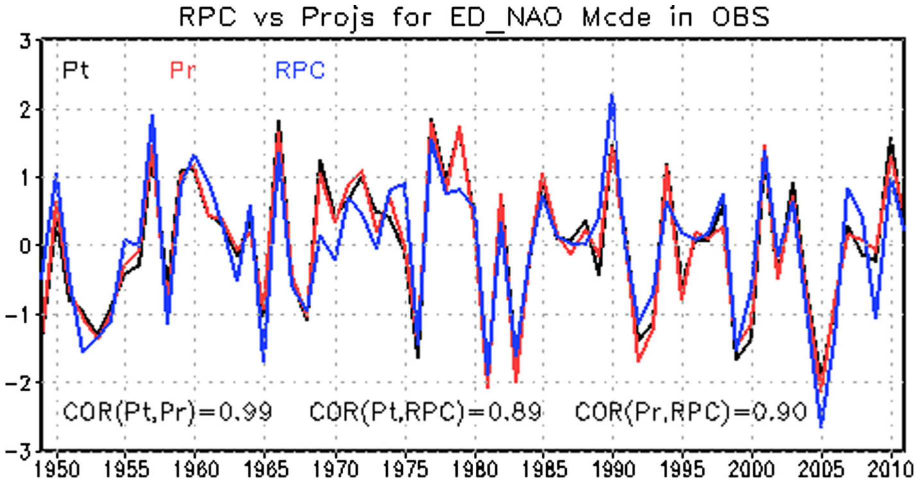

Fig. 12 Normalized time series obtained by projecting ED_NAO patterns to Z200 total fields (*Pt*, *black line*) and residual (*Pr*, *red line*), and the rotated principal component of the mode (*RPC*, *blue line*) for the observation of DJF season over 1949–2011. Also shown are the temporal correlation coefficients between Pt and Pr (0.99), between Pt and RPC (0.89) and between Pr and RPC (0.90)

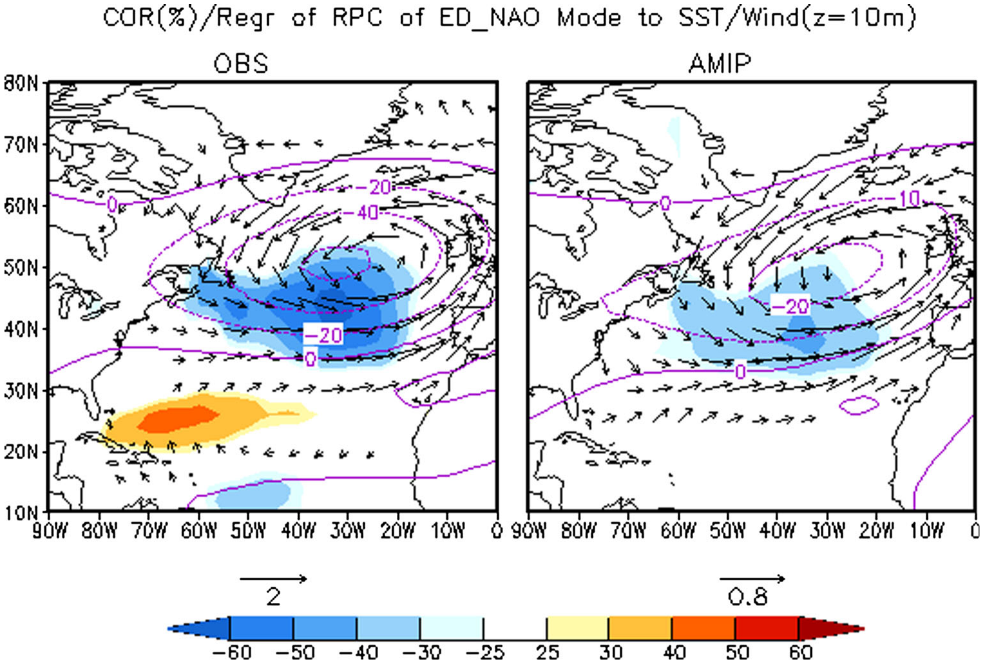

Fig. 13 Correlations of SST (*shadings* in %) and regressions of surface wind (*arrows* in m/s) and Z200 (contours in meters) to the RPC of ED_NAO mode. The *left panel* is for observation and right for AMIP run. The RPC used here for the AMIP results is the ensemble mean of its 12 members as shown with the *red line* in Fig. 11. Ensemble averaging is also applied to surface wind and Z200 before correlation and regression calculation. The areas *shaded* with colors are where the correlations exceed the 95 % significance level in *t* test for degrees of freedom 60

Based on above analyses, it is clear that although in the nature the ED_NAO mode is basically an internal mode, there is a mechanism whereby it can cause SST anomalies, and the SST anomalies in turn can feedback and provide a weak constrain on the atmospheric variability. Comparing to other extratropical modes, such as NAO and PNA, the ED_NAO mode is potentially more predictable and further estimation of its prediction skill needs to be done based on initialized prediction experiments in a fully coupled model.

4 Summary and conclusions

Based on a CMIP, and a set of AMIP runs of the NCEP CFSv2, this study focused on the analysis of the climate mean, variability and dominant patterns of the Northern Hemisphere (NH) wintertime mean Z200 and a comparison to that in observation. For a better understanding of the circulation, the study started with the analysis of SST climatology and the variability of the seasonal mean for the CMIP run and a comparison to observations. Overall, the model SST climate was warmer in the tropical and southern oceans and colder in the NH extratropics. Part of the warming is likely due to the prescribed higher CO_2 concentration. The standard deviation of the DJF mean SST in general was comparable to that in observation, but in the equatorial Pacific Ocean it was somewhat stronger than that in observation. This feature was related to the stronger ENSO variability in the CMIP run.

For the climate mean Z200, it was found that for both the CMIP and AMIP runs, part of the bias in stationary waves, characterized with wave trains emanating from the tropics to both hemispheres, can be attributed to the bias in climate mean precipitation over the Maritime continent. The systematic deficit in latent heating, seen as the precipitation deficit in that area, served as the forcing of the bias in stationary waves. The manifestation of the stationary wave bias in 200 hPa zonal wind is the enhancement and eastward extension of the Pacific jet in the CMIP run, and the southeastward extension of the jet in the AMIP runs.

For the variability of the seasonal mean Z200, both the AMIP and CMIP runs quite successfully simulated the geographical locations of the major centers of action, but the simulated intensity was generally weaker than that in observations, particularly for the center over the Davis Strait-southern Greenland. It is also noted that the simulated centers of action over Aleutian Islands was southeastward shifted to some extent. The shift is likely caused by the eastward extension of the Pacific jet. Differences also existed between the two types of the runs, with the center of action over the Aleutian Islands stronger in the AMIP and the center over the Davis Strait-southern Greenland area stronger in the CMIP simulation.

In the mode analysis, the ENSO teleconnection pattern in each dataset was first removed from the data, a rotated EOF (REOF) analysis was then applied to the residual. The purpose of this separation procedure was to avoid possible mixing between the ENSO mode and those generated by the atmospheric internal dynamics. It was found that the simulated ENSO teleconnection patterns by both types of runs resembled well the observational counterpart, except somewhat eastward shifted for twin anticyclones straddling the equator and a slight southeastward shift of the low center over the North Pacific.

For the REOF modes of the residual data, six dominant modes in observations had their counterparts in each type of run, though with different rankings in explained variance and some distortions in spatial structure. These modes were NAO, PNA, WPO, NA, ED_NAO and TNH modes. Among them, the NAO, NA, ED_NAO and TNH were simulated very well in pattern, with their pattern correlations to that in observation over 0.80. The lower pattern correlations for PNA and WPO modes (between 0.4 and 0.7) were possibly due to their southeastward shift with respect to observations. This shift was likely caused by the eastward or southeastward extension of the climatological Pacific jet in the model.

We also note that each pair of the patterns from two types of runs is almost identical. Because the two types of runs share the same atmospheric model, and have very close spatial structure of stationary waves, the striking mode resemblance between the two simulations suggests that these modes were intrinsic to the atmospheric variability, and the impact from the coupled air-sea interactions was quite limited.

SST influence to the six REOF modes is examined by the temporal coherency between observation and the AMIP run. It is found that ED_NAO mode was the only one with the correlation (=0.44) exceeding the 99 % significance level.

Overall, the NCEP CFSv2 is capable of simulating major features of NH winter season mean circulation with good fidelity. Some distortions in the spatial structure of some dominant modes, such as PNA and WPO patterns, are likely caused by the model bias in its stationary waves. Part of the stationary wave bias likely originated from the mean precipitation bias over the Maritime continent. Thus it can be speculated that an improvement of the precipitation bias in that area could improve model performance in the climate forecast for North America area, and should represent a key target for future model improvements and assessment.

Acknowledgments We would like to thank Drs. Mingyue Chen, Hui Wang for CPC internal reviewing and Z.-Z. Hu and Wanqiu Wang for helpful discussions. We would very appreciate the comments and suggestions from Prof. Edwin Schneider and two anonymous reviewers.

References

Barnston A, Livezey RE (1987) Classification, seasonality and persistence of low-frequency circulation pattern. Mon Weather Rev 115:1083–1126

Branstator G (1992) The maintenance of low-frequency atmospheric anomalies. J Atmos Sci 49:1924–1946

Bretherton CS, Battisti DS (2000) An interpretation of the results from atmospheric general circulation models forced by the time history of the observed sea surface temperature distribution. Geophys Res Lett 27:767–770

DeWeaver E, Nigam S (2004) On the forcing of ENSO teleconnections by anomalous heating and cooling. J Clim 17:3225–3235

Fan M, Schneider E (2012) Observed decadal North Atlantic tripole SST variability. Part I: weather noise forcing and coupled response. J Atmos Sci 69:35–50

Frankignoul C (1985) Sea surface temperature anomalies, planetary waves and air–sea feedback in the middle latitudes. Rev Geophys 23:357–390

Gill A (1982) Atmosphere-ocean dynamics. Academic Press, London

Held IM, Lyons SW, Nigam S (1989) Transients and the extratropical response to El Niño. J Atmos Sci 46:163–174

Held IM, Ting M, Wang H (2002) Northern winter stationary waves: theory and modeling. J Clim 15:2125–2144

Hoerling MP, Kumar A (2002) Atmospheric response patterns associated with tropical forcing. J Clim 15:2184–2203

Hoerling MP, Kumar A, Zhong M (1997) El Niño, La Niña, and the nonlinearity of their teleconnections. J Clim 10:1769–1786

Horel JD (1981) A rotated Principal component analysis of the interannual variability of the northern hemisphere 500 mb height field. Mon Weather Rev 110:2080–2092

Hoskins BJ, James IN, White GH (1983) The shape, propagation and mean-flow interaction of large-scale weather systems. J Atmos Sci 40:1595–1612

Hu Z–Z, Huang B, Pegion K (2008) Low-cloud errors over the southeastern Atlantic in the NCEP CFS and their association with lower-tropospheric stability and air-sea interaction. J Geophys Res 113:D12114. doi:10.1029/2007JD009514

Huang B, Hu Z–Z, Jha B (2007) Evolution of model systematic errors in the tropical Atlantic basin from the NCEP coupled hindcasts. Clim Dyn 28(7/8):661–682. doi:10.1007/s00382-006-0223-8

Jha B, Hu Z–Z, Kumar A (2013) SST and ENSO variability and change simulated in historical experiments of CMIP5 models. Clim Dyn. doi:10.1007/s00382-013-1803-z

Kalnay E et al (1996) The NCEP/NCAR 40-year reanalysis project. Bull Am Meteor 77:437–471

Kang I-S, Lau N-C (1986) Principal modes of atmospheric variability in model atmospheres with and without anomalous sea surface temperature forcing in the tropical Pacific. J Atmos Sci 43:2719–2735

Kumar A, Hoerling MP (2000) Analysis of a conceptual model of seasonal climate variability and implications for seasonal prediction. Bull Amer Meteor Soc 81:255–264

Kumar A, Zhang Q, Peng P, Jha B (2005) SST-forced atmospheric variability in an atmospheric general circulation model. J Clim 18:3953–3967

Kumar A, Chen M, Zhang L, Wang W, Xue Y, Wen C, Marx L, Huang B (2012) An analysis of the nonstationarity in the bias of sea surface temperature forecasts for the NCEP climate forecast system (CFS) version 2. Mon Weather Rev 140:3003–3016

Kushnir Y, Wallace JM (1989) Low-frequency variability in the Norther Hemisphere winter: geographical distribution, structure and time-scale dependence. J Atmos Sci 46:3122–3142

Kushnir Y, Robinson WA, Bladé I, Hall NMJ, Peng S, Sutton R (2002) Atmospheric GCM response to extratropical SST anomalies: synthesis and evaluation. J Clim 16:2233–2256

Linkin ME, Nigam S (2008) The North Pacific Oscillation-West Pacific teleconnection pattern: mature-phase structure and winter impacts. J Clim 21:1979–1997

Mo KC, Livezey RE (1986) Tropical-extratropical geopotential height teleconnections during the northern hemisphere winter. Mon Weather Rev 114:2488–2515

Newman M, Sardeshmukh PD (1998) The impact of the annual cycle on the north pacific/North American response to remote low-frequency forcing. J Atmos Sci 55:1336–1353

Nigam S, Held IM, Lyons SW (1986) Linear simulation of the stationary eddies in a general circulation model. Part I: the no-mountain model. J Atmos Sci 43:2944–2961

Nigam S, Held IM, Lyons SW (1988) Linear simulation of the stationary eddies in a general circulation model. Part II: the "mountain" model. J Atmos Sci 45:1433–1452

O'Lenic A, Livezey RE (1988) Considerations in the use of rotated principal component analysis (RPCA) in diagnostic studies of upper-air height fields. Mon Weather Rev 116:1682–1689

Peña M, Cai M, Kalnay E (2004) Life span of subseasonal coupled anomalies. J Clim 17:1597–1604

Peng P (1995) Dynamics of stationary wave anomalies associated with ENSO in the COLA GCM. Ph.D. thesis, University of Maryland, College Park, 180 pp

Peng P, Kumar A (2005) A large ensemble analysis of the influence of tropical SSTs on seasonal atmospheric variability. J Clim 18:1068–1085

Peng P, Barnston AG, Kumar A (2013) A comparison of skill between two versions of the NCEP climate forecast system (CFS) and CPC's operational short-lead seasonal outlooks. Weather Forecast 28:445–462

Saha S et al (2014) The NCEP climate forecast system version 2. J Clim 27:2185–2208

Sardeshmukh PD, Brian JH (1988) The generation of global rotational flow by steady idealized tropical divergence. J Atmos Sci 45:1228–1251

Smith TM, Reynolds RW, Peterson TC, Lawrimore J (2008) Improvements to NOAA's historical merged land-ocean surface temperature analysis (1880–2006). J Clim 21:2283–2296

Straus DM, Shukla J (2002) Does ENSO Force the PNA? J Clim 15:2340–2358

Ting Mingfang (1996) Steady linear response to tropical heating in Barotropic and Baroclinic models. J Atmos Sci 53:1698–1709

Ting M, Sardeshmukh PD (1993) Factors determining the extratropical response to equatorial diabatic heating anomalies. J Atmos Sci 50:907–918

Trenberth KE, Branstrator GW, Karoly D, Kumar A, Lau N-C, Ropelewski C (1998) Progress during TOGA in understanding and modeling global teleconnections associated with tropical sea surface temperatures. J Geophys Res 103(C7):14291–14324

Van den Dool HM, Peng P, Johansson Å, Chelliah M, Shabbar A, Saha S (2006) Seasonal-to-decadal predictability and prediction of North American climate—the Atlantic influence. J Clim 19:6005–6024

Wallace JM, Blackmon ML (1983) Large-scale dynamical processes in the atmosphere by B. Hoskins and R. Pearce. Academic Press, London, pp 55–91

Wallace JM, Gutzler DS (1981) Teleconnections in the geopotential height field during the Northern Hemisphere winter. Mon Weather Rev 109:784–812

Wang H, Kumar A, Wang W, Xue Y (2012) Influence of ENSO on Pacific decadal variability: an analysis based on the NCEP climate forecast system. J Clim 25:6136–6151

Xie P, Akin PA (1996) Analysis of global monthly precipitation using gauge observations, satellite estimates, and numerical model predictions. J Clim 9:840–858

Xie P, Wang W, Higgins WR, Arkin PA, Cronin M, Weller R (2006) An examination of the bias in the NCEP GFS, CFS simulations associated with the marine stratus clouds. In: AMS 18th conference on climate variability and global change, Jan. 29–Feb. 2, 2006. Atlanta, GA